Excitonic Correlations, Spin-State Ordering, and Magnetic-Field Effects in One-Dimensional Two-Orbital Hubbard Model for Spin-Crossover Region

Koya Kitagawa[1] and Hiroaki Matsueda[2]*

[1]*Department of Physics, Graduate School of Science, Tohoku University*
[2]*Department of Applied Physics, Graduate School of Engineering, Tohoku University*

(Received November 2, 2021)

The electronic properties of excitonic insulators have been examined precisely in recent years. Pictures of exciton condensation may be applied to the spin-state transition observed in perovskite cobalt oxides. We examine the crystal-field and magnetic-field dependences of spatial spin structures on the basis of the density matrix renormalization group method using a low-energy effective model for the one-dimensional two-orbital Hubbard model. We find an excitonic insulating (EI) phase and a spin-state ordering (SSO) phase in the intermediate region between low-spin and high-spin phases. In the EI phase, an excitonic correlation function follows a power law, and an incommensurate spin correlation realizes. In the SSO phase, incommensurate or 3-fold SSO structures realize depending on the crystal-field splitting. these structures are stabilized as a result of the competition of exchange interactions between spin states.

1. Introduction

The spin and orbital degrees of freedom provide a variety of physics in strongly correlated electron systems such as transition metal compounds.[1)] Fe or Co ions in such compounds change their spin states in response to temperature and pressure. For these ions, the competition between the crystal-field splitting and the Hund coupling causes the spin state in the $3d$ orbital to change. $LaCoO_3$ is a typical perovskite cobalt oxide that shows a spin-state transition. The magnetic susceptibility and electrical conductivity of $LaCoO_3$ increase rapidly with temperatures below 100 K.[2,3)]

These temperature dependences are explained by three competing $3d$ electron configurations of the Co^{3+} ion, which are a low-spin state with $S = 0$ for $(t_{2g})^6(e_g)^0$, an intermediate-spin state with $S = 1$ for $(t_{2g})^5(e_g)^1$, and a high-spin state with $S = 2$ for $(t_{2g})^4(e_g)^2$. The competition between these spin states also causes exotic phenomena such as giant magnetoresistance,[4)] magnetic clustering,[5,6)] and ferroelectricity.[7)]

Recently, the possibility of realizing excitonic insulators has been suggested in both experimental and theoretical studies.[8–14)] In excitonic insulators, a macroscopic number of electron-hole pairs are spontaneously generated by Coulomb interaction, and the pairs move coherently. This is called exciton condensation. In the vicinity of the spin-state transition, the fluctuation between competing spin states causes exciton condensation. Therefore, considering the excitonic insulating (EI) phase is important around the spin-state transition.

In the perovskite cobalt oxide $Pr_{0.5}Ca_{0.5}CoO_3$, a first-order metal-insulator phase transition around 90K has attracted attention in regards to the excitonic insulator.[9,15)] A first-order phase transition observed in high-magnetic-field experiments on $LaCoO_3$ has also been discussed in terms of its spin-state transition and exciton condensation.[16–19)] Besides the EI phase, a spin-state ordering (SSO) phase is another candidate for the magnetically induced phase in $LaCoO_3$. In the SSO phase, the spin state is crystallized and shows a superlattice structure. Some spatial patterns have been suggested in numerical analyses.[11,16)] The SSO phase has been observed in $LaCoO_3$ thin films on substrates $[(LaAlO_3)_{0.3}(SrAl_{0.5}Ta_{0.5}O_3)_{0.7}]$, where various superlattice structures of spin states have been observed.[20–22)] In such thin-film experiments, we can vary the spin state by controlling the crystal-field splitting, which are determined by the lattice constant of the substrate.

As described above, in the spin-state transition, the EI phase and the SSO phase can be realized due to the spin and orbital degrees of freedom of $3d$ electrons. To understand the physics in the spin-state transition comprehensively, we need to develop a theory of multi-orbital strongly correlated electron systems that takes into account the various spin structures and exciton condensation.

In this study, we examine the realization of the EI phase and various types of SSO on the basis of numerical analysis of the two-orbital Hubbard model (TOHM), which is the simplest strongly correlated model that describes spin-state transition. In previous theoretical studies, the realization of EI and SSO phases in the two-dimensional (2D) TOHM was confirmed under the framework of mean-field approximation and

*hiroaki.matsueda.c8@tohoku.ac.jp

DMFT.[11,12,23] However, in analyses using these methods, the order parameters or the spatial structures are assumed. In this study, the density matrix renormalization group method (DMRG)[24,25] is performed on a low-energy effective model of the one-dimensional (1D) TOHM. With DMRG, we can perform an accurate analysis with a large system size without any assumptions on the various types of orderings or their spatial structures. Although the dimensionality is limited to 1D due to the limitation of the DMRG, an accurate picture of a 1D quantum system can be a probe for us to understand 2D or 3D ones. The main goal of this study is to make a ground-state phase diagram for the 1D TOHM in the vicinity of spin-state transition and reveal the spatial structure in each phase. Furthermore, we are interested in phenomena peculiar to the 1D system. The phase transition between the SSO phase and the EI phase is interpreted as a localized-itinerant transition for excitons. Thus, quantum-critical phenomena for excitons are expected in the EI phase.

In the analysis of the ground state of the low-energy effective model of TOHM, we find the EI phase and the SSO phase in the intermediate region between the low-spin (LS) phase and the high-spin (HS) phase. In the EI phase, an incommensurate spin correlation occurs, and its characteristic wavenumber changes continuously depending on the amplitude of the crystal field splitting. In the SSO phase, various types of SSO structures are found depending on the crystal-field splitting. As an particularly stable SSO structure, the 3-fold structure of LS/HS/HS is stabilized as a result of competing interactions between the nearest spin states. In the analysis of magnetic-field effects, we find the existence of a Haldane gap not only in the HS phase but also in the EI phase. In the magnetization process in the LS phase, a magnetized EI phase is found. In the magnetization process in the EI phase, we find that the magnetization process is split into two different processes. An analysis of entanglement entropy suggests that the EI phase has an orbital gapless mode.

This paper is organized as follows. In Sect. 2, we derive a low-energy effective model from the TOHM and describe the typical properties of the model. In Sect. 3, we show the results of DMRG analyses: a ground-state phase diagram in Subsect. 3.1, spatial structures of the EI and SSO phases in Subsect. 3.2, a phase diagram in a magnetic field in Subsect. 3.3, and quantum criticality in the EI phase in Subsect. 3.4. In Sect. 4, we summarize the paper.

2. Model and Method

We start with TOHM, which is defined as

$$\begin{aligned}\mathcal{H}_{\mathrm{TOHM}} =& -\sum_{\langle ij\rangle\eta\sigma} t_\eta \left(c^\dagger_{i\eta\sigma}c_{j\eta\sigma} + \mathrm{H.c.}\right) + \Delta\sum_i n_{ia} \\ &+ U\sum_{i\eta} n_{i\eta\uparrow}n_{i\eta\downarrow} + U'\sum_{i\sigma} n_{ia\sigma}n_{ib\sigma} \\ &+ J\sum_{i\sigma\sigma'} c^\dagger_{ia\sigma}c^\dagger_{ib\sigma'}c_{ia\sigma'}c_{ib\sigma} \\ &+ I\sum_{i\eta\neq\eta'} c^\dagger_{i\eta\uparrow}c^\dagger_{i\eta\downarrow}c_{i\eta'\downarrow}c_{i\eta'\uparrow}. \end{aligned} \tag{1}$$

We define the annihilating operator of an electron at site i, orbital $\eta(=a,b)$, and spin $\sigma(=\uparrow,\downarrow)$ as $c_{i\eta\sigma}$. The electron number operator is defined as $n_{i\eta\sigma} = c^\dagger_{i\eta\sigma}c_{i\eta\sigma}$. The first term in Eq. (1) describes the electron hopping between the same orbitals at the nearest sites $\langle ij\rangle$ with its amplitude t_η. The second term describes the crystal-field splitting with its amplitude Δ. The remaining terms represent the intra-site Coulomb interactions, where U is the intra-orbital Coulomb interaction, U' is the inter-orbital Coulomb interaction, J is the Hund coupling, and I is the pair hopping. We use the relational equations for the Coulomb interactions in an isolated ion: $U = U' + 2J$ and $I = J$. We focus on the case in which two electrons exist per site on average.

In the case where t_η in Eq. (1) is small, the low-energy effective Hamiltonian of Eq. (1) is derived by Kanamori et al.[26] by treating the electron hopping terms as perturbations and truncating high-energy bases. The local bases of the effective Hamiltonian are

$$|L\rangle = \left(f c^\dagger_{b\uparrow}c^\dagger_{b\downarrow} - g c^\dagger_{a\uparrow}c^\dagger_{a\downarrow}\right)|0\rangle, \tag{2}$$

$$|H_{+1}\rangle = c^\dagger_{a\uparrow}c^\dagger_{b\uparrow}|0\rangle, \tag{3}$$

$$|H_0\rangle = \frac{1}{\sqrt{2}}\left(c^\dagger_{a\uparrow}c^\dagger_{b\downarrow} + c^\dagger_{a\downarrow}c^\dagger_{b\uparrow}\right)|0\rangle, \tag{4}$$

$$|H_{-1}\rangle = c^\dagger_{a\downarrow}c^\dagger_{b\downarrow}|0\rangle, \tag{5}$$

where $|0\rangle$ is a vacuum. The factors in Eq. (2) are given as $f = 1/\sqrt{1+(\Delta'-\Delta)^2/I^2}$ and $g = \sqrt{1-f^2}$, where $\Delta' = \sqrt{\Delta^2+I^2}$. The state $|L\rangle$ is a low-energy spin singlet state, and $|H_{s^z=0,\pm1}\rangle$ are spin triplet states.

The second order perturbation of t_a and t_b on the on-site basis $\{|L\rangle, |H_{+1}\rangle, |H_0\rangle, |H_{-1}\rangle\}$ gives the following effective Hamiltonian,

$$\begin{aligned}\mathcal{H}^{\mathrm{eff}} =& E_H\sum_i P_{Hi} \\ &+ E_L\sum_i P_{Li} \\ &+ \delta E_{LL}\sum_{\langle ij\rangle} P_{Li}P_{Lj} \\ &+ \delta E_{HL}\sum_{\langle ij\rangle}\left(P_{Hi}P_{Lj} + P_{Li}P_{Hj}\right)\end{aligned}$$

$$+ J_s \sum_{\langle ij \rangle} (\vec{s}_i \cdot \vec{s}_j - 1) P_{Hi} P_{Hj}$$
$$+ J' \sum_{\langle ij \rangle} \left[P_i^- (\vec{s}_i \cdot \vec{s}_j + 1) P_j^+ + \text{H.c.} \right]$$
$$+ I' \sum_{\langle ij \rangle} \left[(\vec{s}_i \cdot \vec{s}_j - 1) P_i^+ P_j^+ + \text{H.c.} \right]. \quad (6)$$

The operators in Eq. (6) are given as

$$P_{Li} = |L\rangle_i \langle L|_i , \quad (7)$$
$$P_{Hi} = \sum_{s^z=-1,0,1} |H_{s^z}\rangle_i \langle H_{s^z}|_i , \quad (8)$$
$$P_i^+ = |H_0\rangle_i \langle L|_i , \quad (9)$$
$$P_i^- = |L\rangle_i \langle H_0|_i . \quad (10)$$

The factors in Eq. (6) are given as

$$E_H = \Delta_a + \Delta_b + U' - J, \quad (11)$$
$$E_L = \Delta_a + \Delta_b + U - \Delta', \quad (12)$$
$$\delta E_{LL} = \frac{4f^2 g^2 (t_a^2 + t_b^2)}{2U' - U - J + 2\Delta'}, \quad (13)$$
$$\delta E_{HL} = (t_a^2 + t_b^2) \left[\frac{f^2}{-\Delta_{ab} + U' + \Delta'} + \frac{g^2}{\Delta_{ab} + U' + \Delta'} \right], \quad (14)$$
$$J_s = \frac{t_a^2 + t_b^2}{U + J}, \quad (15)$$
$$J' = 2t_a t_b \left[\frac{f^2}{-\Delta_{ab} + U' + \Delta'} + \frac{g^2}{\Delta_{ab} + U' + \Delta'} \right], \quad (16)$$
$$I' = 2t_a t_b fg \left[\frac{1}{U + J} + \frac{1}{2U' - U - J + 2\Delta'} \right]. \quad (17)$$

We introduce a spin and pseudospin representation of Eq. (6) to clarify the anisotropy of the Hamiltonian. First, we introduce descending and ascending operators between the $s = 0$ low-spin state and $s = 1$ quadrupoles ($\Gamma = X, Y, Z$), which are defined as

$$P_X^- = \frac{1}{\sqrt{2}} (|L\rangle \langle H_{-1}| - |L\rangle \langle H_{+1}|), \quad (18)$$
$$P_Y^- = \frac{1}{\sqrt{2}i} (|L\rangle \langle H_{-1}| + |L\rangle \langle H_{+1}|), \quad (19)$$
$$P_Z^- = |L\rangle \langle H_0| , \quad (20)$$
$$P_\Gamma^+ = (P_\Gamma^-)^\dagger \quad (\Gamma = X, Y, Z). \quad (21)$$

Second, the pseudospin operators τ_Γ^γ are defined with the descending and ascending operators in Eqs. (18)-(21) as

$$\tau_\Gamma^x = P_\Gamma^- + P_\Gamma^+, \quad (22)$$
$$\tau_\Gamma^y = i(P_\Gamma^- - P_\Gamma^+), \quad (23)$$
$$\tau_\Gamma^z = P_\Gamma^+ P_\Gamma^- - P_L. \quad (24)$$

Note that the representations of the pseudospin operators τ_Γ^γ are twice as much as that of the spin 1/2 operator. Finally, the spin and pseudospin representation of the effective Hamiltonian in Eq. (6) is

$$\mathcal{H}^{\text{eff}} = E_{0\tau} - h_{\tau z} \sum_i \sum_{\Gamma=X,Y,Z} \tau_{\Gamma i}^z + J_s \sum_{\langle ij \rangle} \vec{s}_i \cdot \vec{s}_j + \sum_{\langle ij \rangle} \sum_{\gamma=x,y,z} \sum_{\Gamma=X,Y,Z} J_\gamma \tau_{\Gamma i}^\gamma \tau_{\Gamma j}^\gamma, \quad (25)$$

where $\vec{s}$ is the spin operator whose amplitude is $s = 1$. Note that the spin operator $\vec{s}$ is generally not commutable with the pseudospin operator τ_Γ^γ. The factors in Eq. (25) are given as

$$E_{0\tau} = NE_L - \frac{Nz\delta E_{LL}}{2} + \frac{3N\tilde{\Delta}}{4} + \frac{9NzJ_n}{32}, \quad (26)$$
$$-h_{\tau z} = -\left(\frac{\tilde{\Delta}}{4} + \frac{3zJ_n}{16} \right), \quad (27)$$
$$J_x = \frac{J' + I'}{2}, \quad (28)$$
$$J_y = \frac{J' - I'}{2}, \quad (29)$$
$$J_z = \frac{J_n}{16}, \quad (30)$$

where

$$\tilde{\Delta} = E_H - E_L + z(\delta E_{LL} - \delta E_{HL}), \quad (31)$$
$$J_n = 2\delta E_{HL} - \delta E_{LL} - J_s, \quad (32)$$

where z is number of the nearest sites, and $z = 2$ in the 1D system. In addition to Eq. (25), the Zeeman energy term is introduced as

$$\mathcal{H}_{\text{Zeeman}} = -H \sum_i s_i^z. \quad (33)$$

Before showing the results of the numerical analysis in Sect. 3, we show in Table I typical pseudospins pictures in the effective model in Eq. (25), where spin degrees of freedom and quantum fluctuations are not taken into consideration.

Table I. Typical pseudospins pictures in effective model in Eq. (25).

Phase	τ_Γ Configurations	Parameter conditions
LS	$\downarrow\ \downarrow\ \downarrow\ \downarrow$	$h_{\tau z} \ll 0$ ($\Leftrightarrow \Delta \gg U - U' + J$)
HS	$\uparrow\ \uparrow\ \uparrow\ \uparrow$	$h_{\tau z} \gg 0$ ($\Leftrightarrow \Delta \ll U - U' + J$)
EI	$\rightarrow\ \leftarrow\ \rightarrow\ \leftarrow$	$h_{\tau z} \sim 0$, $J_x > J_y > J_z$ ($\Leftrightarrow \Delta \sim U - U' + J$, $t_a/t_b \sim 1$)
SSO	$\uparrow\ \downarrow\ \uparrow\ \downarrow$	$h_{\tau z} \sim 0$, $J_x, J_y \ll J_z$ ($\Leftrightarrow \Delta \sim U - U' + J$, $t_a/t_b \sim 0$)

In the case of $\Delta \gg U - U' + J$, where the crystal-field splitting is sufficiently large, $h_{\tau z} \ll 0$ in the effective model in Eq. (25), and the ground state is in a low-spin (LS) phase with $(\tau_\Gamma : \downarrow \downarrow \ \ldots \ \downarrow)$. In the case of $\Delta \ll U - U' + J$, $h_{\tau z} \gg 0$, and the ground state is in a high-spin (HS) phase with $(\tau_\Gamma : \uparrow \uparrow \ \ldots \ \uparrow)$. Because of the spin-spin interaction in Eq. (25), the spins in the HS phase form an anti-ferromagnetic structure with $(s : \uparrow \downarrow \ \ldots \ \uparrow \downarrow)$. In the case where the amplitude of Δ and $U - U' + J$ are competing, the inter-pseudospin interaction J_γ and the inter-spin interaction J_s are dominant. The inter-pseudospin interaction J_γ is anisotropic for $\gamma = x, y, z$. Since $J_z \propto t_a^2 + t_b^2$ and $J_x, J_y \propto 2t_a t_b$, the behavior of the ground state changes depending on the parameter $\eta = 2t_a t_b/(t_a^2 + t_b^2)$, which characterizes the anisotropy. The range of η is $0 \le \eta \le 1$, where $t_a/t_b = 0$ for $\eta = 0$, and $t_a/t_b = 1$ for $\eta = 1$. In the case of $\eta \ll 1$, the anisotropy becomes $J_z \gg J_x, J_y$, and the ground state tends to show a spin-state ordering (SSO) with $(\tau_\Gamma : \uparrow \downarrow \ \ldots \ \uparrow \downarrow)$. If η is sufficiently large, the anisotropy becomes $J_z < J_y < J_x$, and pseudospins tend to form a state in which the pseudospin points in the x axis, $(\tau_\Gamma : \rightarrow \leftarrow \ \ldots \ \rightarrow \leftarrow)$. This state is interpreted as the EI state, where the LS state and HS state are hybridized. In practice, the picture of the ground state of the effective model becomes more complicated due to the competition of multiple interactions in Eq. (25).

We apply the density matrix renormalization group method (DMRG) to the effective model. The system is 1D and has an open boundary condition unless otherwise specified. We set the truncation number in DMRG to $\chi = 256$ (and exceptionally $\chi = 64$ for determining some phase boundaries). Under this setting, the truncation error of the reduced density matrix is less than 10^{-5}. We additionally use a periodic boundary condition for analyses of the SSO phase, where incommensurate spin structures are found.

3. Results

3.1 Ground-state phase diagram

In this subsection, we present phase diagrams obtained by the numerical analysis with DMRG.

First, we fix the anisotropy factor for the pseudospin interaction at $\eta = 1\,(\Leftrightarrow t_a = t_b)$ and make a phase diagram in the plane of the crystal-field splitting Δ and the amplitude of Hund coupling J, where we set the parameters of the Coulomb interactions as $U/\sqrt{t_a^2 + t_b^2} = 12$, $U' = U - 2J$, and $J = I$ as a strongly correlated region. The Δ-J phase diagram is shown in Fig. 1(a). In Fig. 1(a), as Δ increases, the phase shifts as HS $\rightarrow$ EI $\rightarrow$ LS, where HS, EI, and LS stand for a low-spin phase, an excitonic insulating phase, and a high-spin phase respectively. The phase transitions at HS-EI and EI-LS are second-order transitions. We obtain the phase boundary by the discontinuity of the entanglement entropy, which is discussed in Subsect. 3.4.

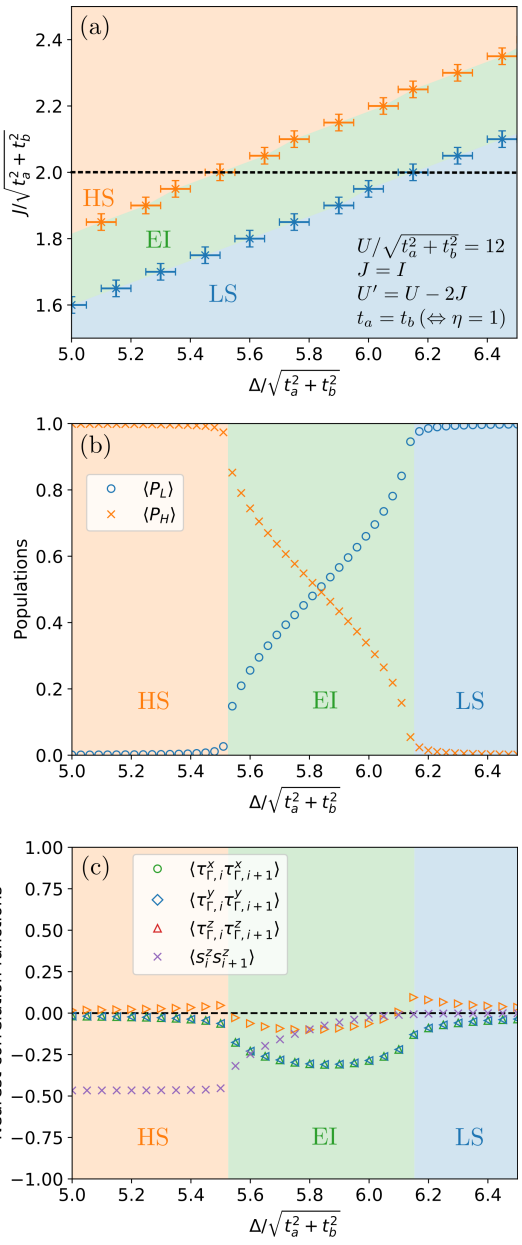

Fig. 1. Panel (a) shows a ground-state phase diagram for the effective Hamiltonian in Eq. (25) in the plane of the Hund coupling $J/\sqrt{t_a^2 + t_b^2}$ and the crystal-field splitting $\Delta/\sqrt{t_a^2 + t_b^2}$, where we fix the intra-orbital Coulomb interactions to $U/\sqrt{t_a^2 + t_b^2} = 12$, and the anisotropy factor in the exchange interaction is chosen to be $\eta = 1\,(\Leftrightarrow t_a = t_b)$. Panel (b) shows the populations of the LS and HS states along the dashed line in panel (a), where $J/\sqrt{t_a^2 + t_b^2} = 2$. Panel (d) shows the nearest correlation functions along the dashed line in Panel (a).

In Fig. 1(b), we present the populations of the HS state $\langle P_H \rangle$ and LS state $\langle P_L \rangle$ along the dashed line in Fig. 1(a). The population of the LS state increases in the EI phase as Δ increases.

Here, we note that spontaneous symmetry breakings

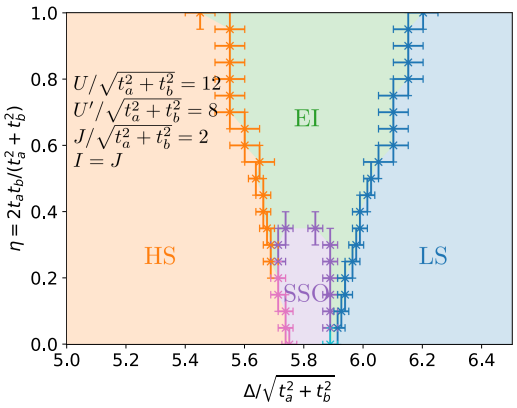

Fig. 2. A ground-state phase diagram for the effective Hamiltonian in Eq. (25) in the plane of the anisotropy factor for pseudospin η and the crystal-field splitting $\Delta/\sqrt{t_a^2+t_b^2}$, where we fix that $U/\sqrt{t_a^2+t_b^2}=4$ and $J/\sqrt{t_a^2+t_b^2}=2$. The error bars represent discrete intervals for the analysis.

are not obtained in the EI phase for neither spins nor pseudospins, that is, $\langle\tau^x_{\Gamma,i}\rangle=\langle\tau^y_{\Gamma,i}\rangle=0$ for $\Gamma=X,Y,Z$ and $\langle s^\gamma_i\rangle=0$ for $\gamma=x,y,z$. Alternatively, the power law for the excitonic correlation is obtained in the EI phase as $|\langle\tau^x_{\Gamma i}\tau^x_{\Gamma j}\rangle|=(i-j)^\alpha$, which is presented in Subsect. 3.4 in detail. We can understand the property of the EI phase in the nearest correlation functions. We show the nearest correlation functions, $\langle\tau^x_{\Gamma i}\tau^x_{\Gamma i+1}\rangle$, $\langle\tau^y_{\Gamma,i}\tau^y_{\Gamma,i+1}\rangle$, $\langle\tau^z_{\Gamma,i}\tau^z_{\Gamma,i+1}\rangle$, and $\langle s^z_i s^z_{i+1}\rangle$, in Fig. 1(c). Note that the product of the nearest pseudospin, $\langle\tau^z_{\Gamma i}\rangle\langle\tau^z_{\Gamma i+1}\rangle$, is not subtracted from $\langle\tau^z_{\Gamma i}\tau^z_{\Gamma i+1}\rangle$ although $\langle\tau^z_{\Gamma j}\rangle$ is positive in the HS phase and negative in the LS phase. We compute the correlation function at the center of the system. The values of the pseudospin correlations are independent of the quadruple basis $\Gamma=X,Y,Z$ because of the rotational symmetry. The correlation functions in the EI phase give $\langle\tau^x_{\Gamma,i}\tau^x_{\Gamma,i+1}\rangle<\langle\tau^y_{\Gamma,i}\tau^y_{\Gamma,i+1}\rangle<\langle\tau^z_{\Gamma,i}\tau^z_{\Gamma,i+1}\rangle$ corresponding to the anisotropy $J_x>J_y>J_z$ at $\eta=1$ ($\Leftrightarrow t_a=t_b$). The large values of $|\langle\tau^x_{\Gamma,i}\tau^x_{\Gamma,i+1}\rangle|$ in the EI phase correspond to the trend of the triplet exciton condensation, where the HS state moves coherently. The nearest spin correlation $\langle s^z_i s^z_{i+1}\rangle$ in Fig. 1(c) is anti-ferromagnetic in the HS and EI phases. In the HS phase, the Hamiltonian in Eq. (25) is reduced to the $s=1$ Heisenberg model, and the ground state gives the anti-ferromagnetic correlation.

Next, we present a phase diagram in the plane of the anisotropy for the pseudospin interaction η and the crystal-field splitting Δ in Fig. 2, where we fix the parameters of Coulomb interactions to $U/\sqrt{t_a^2+t_b^2}=12$, $U'/\sqrt{t_a^2+t_b^2}=8$, and $J/\sqrt{t_a^2+t_b^2}=I/\sqrt{t_a^2+t_b^2}=2$. In addition to the HS, EI, and LS phases, the spin-state ordering (SSO) phase is found in Fig. 2. In the SSO phase, the population of HS states varies from site to site. The spatial structure of SSO changes according to Δ and η, including the 3-fold structure of LS/HS/HS as an especially stable structure. This SSO structure is different from the results of mean-field analyses.[10,11] We focus on the spatial structures in the next subsection.

We characterize the SSO phase on the basis of the spontaneous symmetry breaking of the spatial spin-state structure in the formulation of the DMRG analysis. The criterion is that a state is in the SSO phase when $\max(\langle P_{Hi}\rangle)-\min(\langle P_{Hi}\rangle)>10^{-2}$ for i in the central 20 sites in a system whose sizes are $L=60$.

The outlines in the phase diagrams in Fig. 1 and Fig. 2 can be understood as the typical behavior of pseudospins, which is shown in Table I and consistent with the previous studies.[10,19] However, no spin or pseudospin ordering is observed in the HS and EI phases. This is interpreted as the result of the effect of strong quantum fluctuations in the 1D system, which is considered in the DMRG method. In addition, various types of spin-state structures were obtained by using large 1D clusters.

3.2 Spatial structures of spin states in the EI and SSO phases

In this subsection, we present the spatial structures of the spin states in the EI phase and the SSO phase through correlation functions. We set the system size as $L=60$ and use the periodic boundary condition. The truncation number in DMRG is set as $\chi=256$.

We consider a Fourier transformed correlation functions for spin states as

$$C_X(k)=\frac{1}{L}\sum_{ij}\langle X_iX_j\rangle\cos\left[k(i-j)\right], \qquad (34)$$

where X_i is a one-site operator at a site i. Note that the product of one-site expected values are not subtracted in $C_X(k)$.

First, we fix the parameters as $U/\sqrt{t_a^2+t_b^2}=12, J/\sqrt{t_a^2+t_b^2}=I/\sqrt{t_a^2+t_b^2}=2, U'=U-2J, \eta=0.5$. In this region, the phase transition is HS $\rightarrow$ EI $\rightarrow$ LS as $\Delta/\sqrt{t_a^2+t_b^2}$ increases.

In Fig. 3(a), we present the correlation function for the HS state $C_{P_H}(k)$ in the EI phase. Since $\langle P_{Hi}\rangle$ is uniform in the EI phase, $C_{P_H}(k)$ means the fluctuation in the population of the HS state except for $C_{P_H}(k=0)$, which originates in the uniform populations of the HS state. $C_{P_H}(k\neq0)$ is small in the HS phase and the LS phase and becomes large in the EI phase. In the EI phase, $C_{P_H}(k)$ tends to rise in $k<\min(2\pi\langle P_H\rangle, 2\pi(1-\langle P_H\rangle))$ and becomes constant in $k>\min(2\pi\langle P_H\rangle, 2\pi(1-\langle P_H\rangle))$, where $\langle P_H\rangle$ is the spatial average of the population of the HS state. $\langle P_H\rangle$ is determined by the amplitude of crystal-field splitting $\Delta/\sqrt{t_a^2+t_b^2}$. This behavior is similar to the number operator correlation in Tomonaga-Luttinger liquid (TLL). As a difference from the TLL, $C_{P_H}(k\rightarrow0)$ has finite values in the EI phase. This is because $\sum_i P_{Hi}$ is gen-

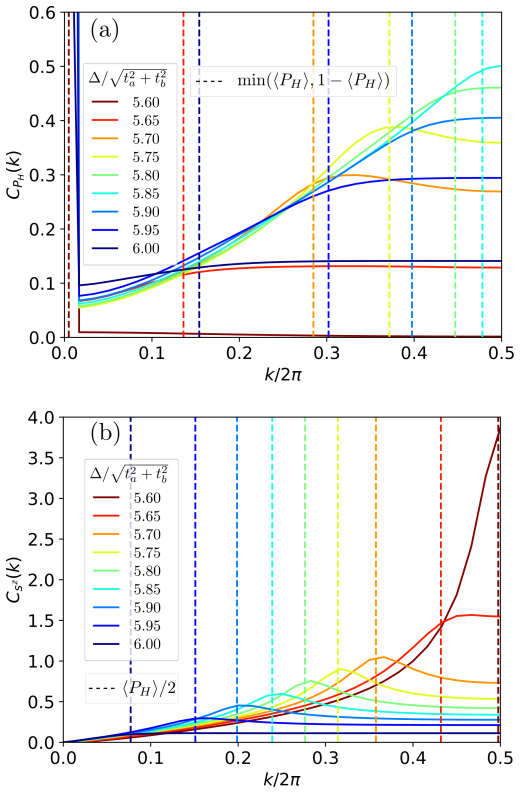

Fig. 3. Fourier transformed correlation functions in the EI phase. Panel (a) shows the correlations of HS state $C_{P_H}(k)$ at $\eta = 0.5$ for some $\Delta/\sqrt{t_a^2+t_b^2}$. The dashed lines in panel (a) are the expected values of $\min(\langle P_H\rangle, 1-\langle P_H\rangle)$ per site. Panel (b) shows the spin correlation $C_{s^z}(k)$ at $\eta = 0.5$. The dashed lines in panel (b) are $\langle P_H\rangle/2$.

erally not commutative with the Hamiltonian due to the pair hopping term in Eq. (25). These behaviors of $C_{P_H}(k)$ indicate that the HS state behaves as an itinerant quasiparticle in the EI phase. We can find the peaks in $\Delta/\sqrt{t_a^2+t_b^2} = 5.75, 5.80$ lines in Fig. 3. These peaks are interpreted as a precursor to the SSO.

In Fig. 3(b), we show the Fourier transformed spin correlation $C_{s^z}(k)$ with the same parameters as in Fig. 3(a). $C_{s^z}(k)$ has a peak at $k = \pi\langle P_H\rangle$ in the EI and HS phases. This is interpreted as the spin correlation in the EI phase representing a spin density wave whose wavenumber corresponds to the population of the HS state, although there is no spin ordering.

Next, we fix $\eta = 0.3$. In this region, the phase transitions are HS $\to$ EI $\to$ SSO $\to$ EI $\to$ LS as $\Delta/\sqrt{t_a^2+t_b^2}$ increases. Figure 4(a) shows $C_{P_H}(k)$ in the SSO phase. We also show the peak wavenumbers against the crystal-field splitting in Fig. 4(b). The sharp peaks in Fig. 4(a) represent the structure of the SSO. There is a strong peak for $k = 2\pi/3$ in $\Delta/\sqrt{t_a^2+t_b^2} = 5.75$. This peak represents the LS/HS/HS structure shown in Fig. 4(d).

As shown in Fig. 4(b), the spin-state structure in

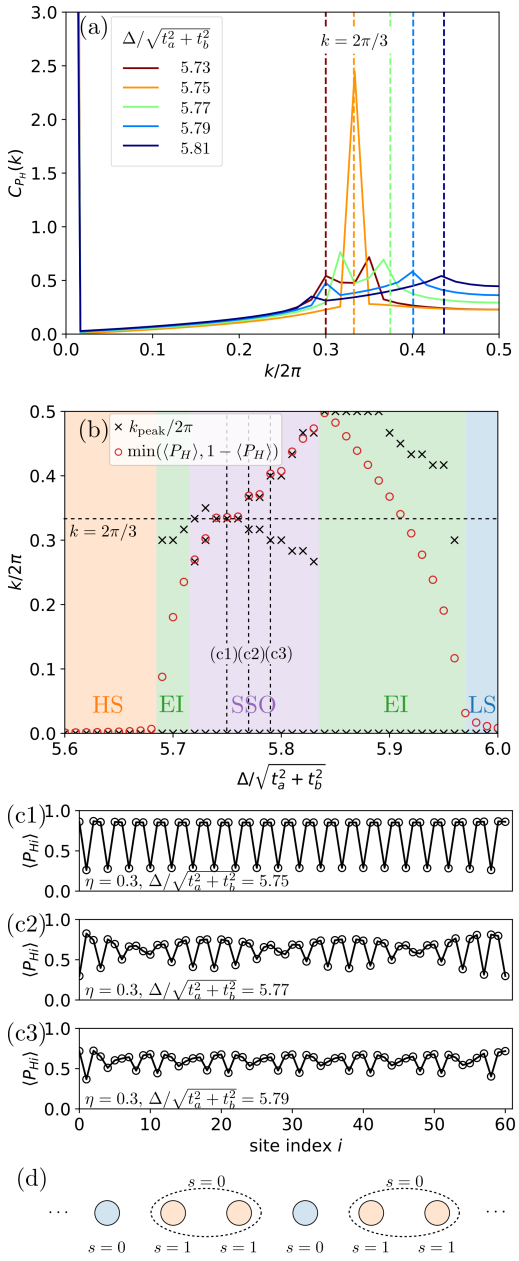

Fig. 4. Fourier transformed correlation functions in the SSO phase. Panel (a) shows the correlations of HS state $C_{P_H}(k)$ at $\eta = 0.3$ for some $\Delta/\sqrt{t_a^2+t_b^2}$. The dashed lines are the expected values of $\min(\langle P_H\rangle, 1-\langle P_H\rangle)$. Panel (b) shows the peak wavenumber against the crystal-field splitting $\Delta/\sqrt{t_a^2+t_b^2}$. In Panels (c1), (c2), and (c3), some SSO structures obtained in the SSO phase are shown. Each parameter corresponds to the dashed line in panel (b). Panel (d) shows the schematic picture of the LS/HS/HS structure in Panel (c1).

the SSO phase changes against the crystal-field splitting $\Delta/\sqrt{t_a^2+t_b^2}$. The plateau at $k = 2\pi/3$ in Fig. 4(b) indicates that the LS/HS/HS structure is stable. According to the Hamiltonian in Eq. (25), the nearest LS-HS pair is stabilized by the J_z term, and the nearest HS-HS pair

is stabilized by the J_s term. The LS/HS/HS structure is realized as a result of the competition between these interactions. In the other region in the SSO phase, two peaks branch from the peak at $k = 2\pi/3$. The two peaks have generally incommensurate wavenumbers, and one of them follows the population of the HS state $\langle P_H \rangle$. The discretization of the $k_{\rm peak}$ in Fig. 4(b) is assumed to originate from the finite system size $L = 60$ and should become continuous in $L \to \infty$. Some snapshots of the spin-state structures in the SSO phase are shown in Fig. 4(c1)-(c3). Figure 4(c1) shows the LS/HS/HS structure shown in Fig. 4(d). Figure 4(c2) shows the structure near the LS/HS/HS structure, where some kinks are inserted into the basic LS/HS/HS structure. Figure 4(c3) is the structure far from the parameter shows the LS/HS/HS, where a complex spin state is found. We cannot find the SSO phase in the region where $\langle P_H \rangle < 0.5$ in this region. The result indicates that the spin-spin interaction between the HS states contributes to the stabilization of the SSO with the LS/HS/HS structure.

3.3 Magnetic-field effects

In this subsection, we present the magnetic-field effects in the effective model. Figures 5(a) and 5(b) are phase diagrams in the plane of the crystal-field splitting $\Delta/\sqrt{t_a^2+t_b^2}$ and the magnetic field $H/\sqrt{t_a^2+t_b^2}$, where we fix the parameters, $U/\sqrt{t_a^2+t_b^2} = 12$, $J/\sqrt{t_a^2+t_b^2} = I/\sqrt{t_a^2+t_b^2} = 2$, $U' = U - 2J$ and $\eta = 1\,(\Leftrightarrow t_a = t_b)$, where the EI phase exists in the intermediate region between the HS and LS phases. In Figs.5(a) and 5(b), in addition to the HS, EI, and LS phases, there appears a type-1 magnetized excitonic insulating phase (MEI-1), a type-2 magnetized excitonic insulating phase (MEI-2), a magnetized high-spin phase (MHS), and a fully polarized phase (Full Polar). All the phase transitions are second-order ones. We determine the phase boundary on the basis of the discontinuity of the first derivative of the magnetization curve. In the MEI-1 and MEI-2 phases, hybridization of the LS state and HS state are found and the power law of $|\langle \tau^x_{Xi}\tau^x_{Xj}\rangle| = |i-j|^\alpha$ is obtained. Basically, we use an $L = 60$ cluster and set the truncation number in DMRG to $\chi = 64$. To precisely determine the spin gaps, the phase boundaries for HS-MHS and EI-MEI-2 are determined by the system-size extrapolations. The extrapolation is performed with the function $\Delta_s(1/L) = \Delta_s(0) + a/L + b/L^2$, where $\Delta_s(0)$, a and b are the fitting parameters, and $\Delta_s(0)$ is a spin gap in the infinite system. We use the system size $L = 64, 128, 192, 256$ under the open boundary condition and set the truncation number in DMRG to $\chi = 256$.

As shown in Figs.5(a) and 5(b), spin gaps are obtained in the LS, EI, and HS phases. In the LS phase, there is a spin gap due to the energy difference between the LS state and the HS state. The spin gap in the EI phase is connected to the spin gap in the HS phase and becomes smaller as $\Delta/\sqrt{t_a^2+t_b^2}$ approaches the LS phase and finally closes at the phase boundary between the EI and LS phases.

The spin gap in the HS phase is the Haldane-gap because in the region where $\Delta \ll U - U' + J$, the low-energy effective Hamiltonian in Eq. (25) reduces to the $s = 1$ Heisenberg model. The magnetic property in the EI phase is similar to the $s = 1$ Heisenberg model. In addition to the existence of the spin gap, the ground state in the EI phase has quadruple degeneracy, which is also found in the ground state in the $s = 1$ Heisenberg model under the open boundary condition. From this behavior, the spin gap in the EI phase is considered to be a spin gap peculiar to the 1D system.

From here, we present the magnetization processes in the phases along the dashed lines (c)-(h) in Fig. 5(a).

The magnetization process in a wide range of the HS phase is HS→ MHS → Full Polar (the dashed line at (c) and (d) in Fig. 5(a)). In the MHS phase, the population of the LS state is almost zero and $\langle \tau^x_{\Gamma,i}\tau^x_{\Gamma,i+1}\rangle$ is almost zero.

The magnetization process in the EI phase is EI→MEI-2→MEI-1→Full Polar (the dashed line at (e) and (f) in Fig. 5(a)), where we call the phase in the low magnetic field MEI-2 and the phase in the high magnetic field MEI-1. In the MEI-2 phase, the population of the HS state is finite for all quadrupole bases of X, Y, and Z. In the MEI-1 phase, the populations of X and Y are finite, and that of Z becomes zero. Since $|H_{s^z=+1}\rangle = -(P^+_{H_X}|L\rangle + iP^+_{H_Y}|L\rangle)/\sqrt{2}$, the X and Y excitons coexist with the z-direction magnetization, while the Z excitons compete with the z-direction magnetization. This difference results in the separation between the MEI-2 phase and the MEI-1 phase. In fact, in the MEI-2 phase, none of the populations of the $(s = 1, s^z = -1)$ state, $(s = 1, s^z = 0)$ state, $(s = 1, s^z = +1)$ state, and $(s = 0, s^z = 0)$ state are zero. The populations of the $(s = 1, s^z = -1)$ state and the $(s = 1, s^z = 0)$ state almost reached zero at the phase boundary between the MEI-2 phase and the MEI-1 phase. The nearest correlation functions in the magnetization process in the EI phase in Fig. 5(f) show that $\langle \tau^x_{Z,i}\tau^x_{Z,i+1}\rangle$ becomes almost zero at the phase boundary between the MEI-2 and MEI-1 phases while $\langle \tau^x_{X,i}\tau^x_{X,i+1}\rangle$ and $\langle \tau^x_{Y,i}\tau^x_{Y,i+1}\rangle$ are finite even in the MEI-1 phase. These results indicate that the MEI-1 phase is stabilized by the kinetic energy of the $(s = 1, s^z = +1)$ excitons, while the MEI-2 phase is stabilized by the kinetic energy of all of the X, Y, and Z excitons.

The magnetization process in the LS phase is LS→MEI-1→Full Polar (the dashed line at (g) and (h) in Fig. 5(a)). The MEI-1 phase is the same phase as in the magnetization process in the EI phase. As shown in Figs. 5(g) and 5(h), the $(s = 1, s^z = 0)$ state and $(s = 1, s^z = -1)$ state are almost zero in the whole magnetization process in the LS phase.

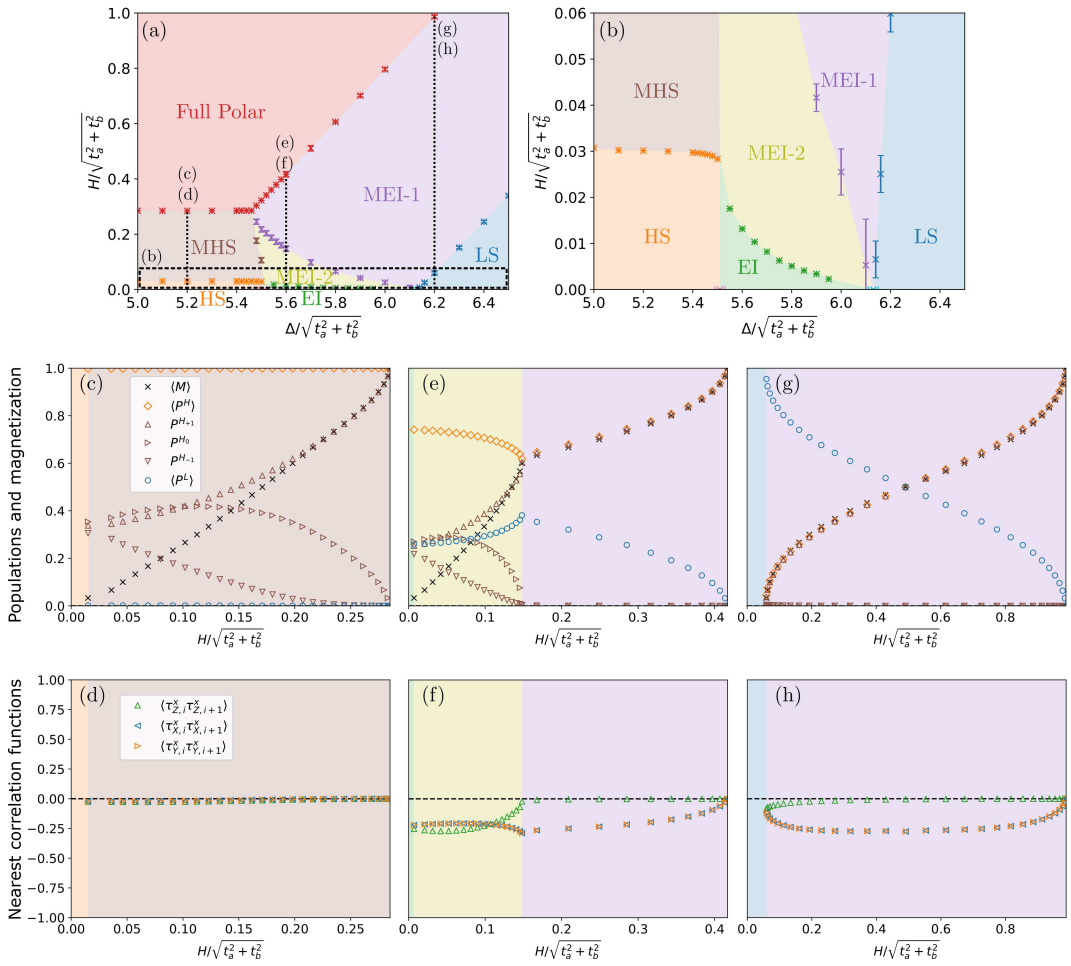

Fig. 5. Phase diagram of the effective model in a magnetic field. Panel (a) is phase diagram in the magnetic field $H/\sqrt{t_a^2+t_b^2}$ and crystal-field splitting $\Delta/\sqrt{t_a^2+t_b^2}$. Panel (b) is the enlarged view of the low magnetic-field region enclosed by the dashed line in panel (a). The error bars in Panels (a) and (b) represent the discretization of the magnetization in the finite system size $L = 60$. Exceptionally, the phase boundaries at the HS-MHS and the EI-MEI-2 are determined by the extrapolation, and the errors are smaller than the size of points. The dashed line in panel (a) represents the magnetization process in each phase in panels (c)-(h). Panels (c), (e), and (g) shows the magnetization curve and the populations of spin states in the magnetization process in the HS, EI, and LS phases, respectively. Panels (d), (f), and (h) show nearest spin correlation and nearest pseudospin correlations in the magnetization process in the HS, EI, and LS phases, respectively.

In Fig. 5(a), we presented the magnetic-field effects around the EI phase, where $\eta = 1\,(\Leftrightarrow t_a = t_b)$. The magnetic field effects for smaller η are left for future work, where the magnetized SSO phase may be found because the LS/HS phase was obtained under a magnetic field with a mean-field analysis.[11)]

3.4 Criticality

In this subsection, we present the criticality of the EI phase. Since the EI phase is expected to be a critical one, it is better to evaluate the logarithmic scaling of the entanglement entropy and the corresponding central charge. Fig. 6(a) shows the entanglement entropy as a function of crystal-field parameters, where we divide the system whose size is $L = 60$ into a left one and right one whose size is $l = 30$. The truncation number in DMRG is set as $\chi = 256$ for Fig. 6. We set $\eta = 1.0\,(\Leftrightarrow t_a = t_b)$, $U/\sqrt{t_a^2+t_b^2} = 12$, $U' = U - 2J$ and $J = I$, which are the same as the parameters in the dashed line in Fig. 1(a).

In the HS phase, the ground state is a valence bond solid in the $s = 1$ Heisenberg model. The entanglement entropy in the HS phase is about $2\log 2 \simeq 1.39$. The $\log 2$ originate in the singlet forming a valence bond, and the other $\log 2$ is due to the edge state, where the $1/2$ spins at both edges form a singlet. In the EI phase, the entropy becomes large. The discontinuities in the phase boundaries are used when we determine the HS-EI and EI-LS phase boundaries in Fig. 1 and Fig. 2. In the LS phase, the entropy is quite small. This is because the electrons in the LS phase cannot move due to the Pauli

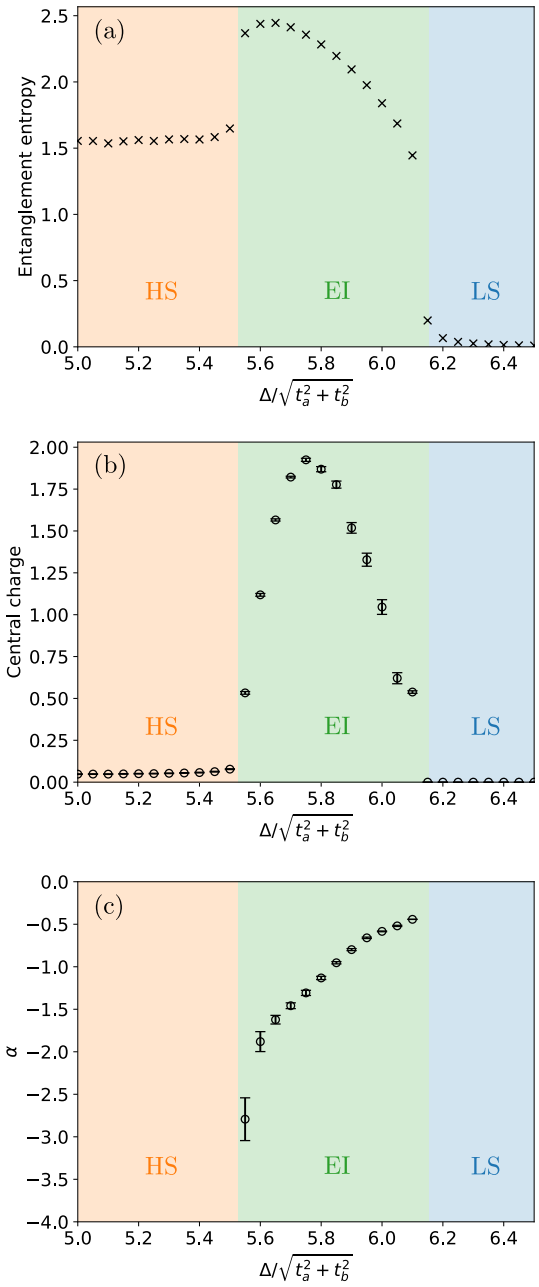

Fig. 6. Criticality in the EI phase. Panel (a) shows the entanglement entropy in the HS, EI and LS phases. Panel (b) shows the estimated central charges.. Panel (c) shows the critical exponent α in the EI phase for $|\langle\tau^x_{\Gamma,i}\tau^x_{\Gamma,j}\rangle| \propto |i-j|^{\alpha}$

exclusion principle.

Fig. 6(b) is the value of the central charge estimated from the formula in a 1D quantum-critical system:[27]

$$S(l) = (c/6)\log\left[(L/\pi)\sin(\pi l/L)\right] + \text{const.}, \qquad (35)$$

where $S(l)$ is the entanglement entropy where a system whose size is L is divided into a left one whose size is l and a right one whose size is $L-l$.

Since the LS phase and the HS phase are gapped, the central charges are estimated to be 0 in Fig. 6. In the EI phase, the value of the central charge is maximum in the middle of the EI phase. The finite central charge in the EI phase suggests that the EI phase is a quantum-critical phase. The behavior of the central charge in Fig. 6(b) is different from the case of the extended Falicov-Kimball model, where the central charge in the EI phase is constant at 1.[28] In the case of TOHM, there are spin degrees of freedom, and the EI phase is a triplet one. In addition, anti-ferromagnetic interactions interfere with the motion of the excitons. These effects are interpreted as the reason why the central charge changes in the range of 0 to 2 in the EI phase.

We present the power law in the correlation function for the EI phase. Since there are energy gaps in the HS and LS phases, there are no correlation functions that follow the power law. For the EI phase in Fig. 6(b), the central charge is finite, and it is expected that there is a correlation function that behaves critically. We obtain the power law for the excitonic correlation as $\langle\tau^x_{\Gamma i}\tau^x_{\Gamma j}\rangle \propto |i-j|^{\alpha}$. The critical exponent α in the EI phase is shown in Fig. 6(c), where we evaluate the critical exponent α by fitting. The critical exponent changes against $\Delta/\sqrt{t_a^2+t_b^2}$ and the excitonic correlation reaches farther near the LS phase. For other correlation functions, we find that the $\langle s^z_i s^z_j\rangle$ has exponential decay. $\langle P^H_i P^H_j\rangle$ and $\langle\tau^y_{\Gamma,i}\tau^y_{\Gamma,j}\rangle$ may follow a power law, but since these correlation functions have incommensurate structures and have strong finite-size effects, we cannot estimate the critical exponent.

In the EI phase, the charge gap is open because the onsite Coulomb interaction fixes the number of electrons per site to 2. The spin gap is also open according to the DMRG analysis in Subsect. 3.3. Therefore the gapless mode in the EI phase originates purely in the orbital degrees of freedom, which does not coupled with electric fields nor a magnetic field.

4. Summary

We made a ground-state phase diagram of the low-energy effective model of the one-dimensional two-orbital Hubbard model for the spin-crossover region on the basis of the density matrix renormalization group method. We found an excitonic insulating (EI) phase and spin-state ordering (SSO) phase in the intermediate region between a low-spin (LS) phase and a high-spin (HS) phase. The EI phase is realized in the region where $t_a/t_b \sim 1$, where t_a/t_b is the ratio of electron transfers, and the SSO phase is realized in the region where $t_a/t_b \ll 1$.

The spin correlation function in the EI phase has a peak wavenumber at $k = \pi\langle P_H\rangle$, resulting in a incommensurate spin correlation. The spin-state structure in the SSO phase show the LS/HS/HS structure and various types of incommensurate structures depending on the crystal-field splitting.

We also made a phase diagram in the magnetic field.

We found a spin gap not only in the LS and HS phases but also in the EI phase. The spin gap found in the EI phase is similar to the Haldane gap observed in the $s = 1$ Heisenberg model. We also found that the magnetization process in the EI phase has two stages, where the magnetization curve has different gradients corresponding to the different types of excitonic insulating phases.

Finally, we showed the quantum-critical behavior in the EI phase from the viewpoint of entanglement entropy. The breaking of the area law of the entanglement entropy was found in the EI phase, and the central charge changes continuously. This result and the existence of the spin and charge gaps indicate the existence of an orbital gapless mode that does not couple with an electric field nor a magnetic field.

Acknowledgements

We are grateful to M. Naka, J. Nasu, A. Ono, and Y. Masaki for their fruitful discussion and critical readings of the manuscripts. H. M. also acknowledges financial support from KAKENHI No. 18K03474.

1) M. Imada, A. Fujimori, and Y. Tokura: Rev. Mod. Phys. **70** (1998) 1039.
2) S. Yamaguchi, Y. Okimoto, H. Taniguchi, and Y. Tokura: Phys. Rev. B **53** (1996) R2926.
3) K. Asai, A. Yoneda, O. Yokokura, J. Tranquada, G. Shirane, and K. Kohn: J. Phys. Soc. Jpn. **67** (1998) 290.
4) R. Mahendiran and A. K. Raychaudhuri: Phys. Rev. B **54** (1996) 16044.
5) K. Sato, A. Matsuo, K. Kindo, Y. Kobayashi, and K. Asai: J. Phys. Soc. Jpn. **78** (2009) 093702.
6) J. Yu, D. Louca, D. Phelan, K. Tomiyasu, K. Horigane, and K. Yamada: Phys. Rev. B **80** (2009) 052402.
7) K. Oka, M. Azuma, W.-t. Chen, H. Yusa, A. A. Belik, E. Takayama-Muromachi, M. Mizumaki, N. Ishimatsu, N. Hiraoka, M. Tsujimoto, M. G. Tucker, J. P. Attfield, and Y. Shimakawa: J. Am. Chem. Soc. **132** (2010) 9438.
8) J. Kuneš and P. Augustinský: Phys. Rev. B **89** (2014) 115134.
9) J. Kuneš and P. Augustinský: Phys. Rev. B **90** (2014) 235112.
10) J. Nasu, T. Watanabe, M. Naka, and S. Ishihara: Phys. Rev. B **93** (2016) 205136.
11) T. Tatsuno, E. Mizoguchi, J. Nasu, M. Naka, and S. Ishihara: J. Phys. Soc. Jpn. **85** (2016) 083706.
12) D. Geffroy, A. Hariki, and J. Kuneš: Phys. Rev. B **97** (2018) 155114.
13) Y. Wakisaka, T. Sudayama, K. Takubo, T. Mizokawa, M. Arita, H. Namatame, M. Taniguchi, N. Katayama, M. Nohara, and H. Takagi: Phys. Rev. Lett. **103** (2009) 026402.
14) K. Seki, Y. Wakisaka, T. Kaneko, T. Toriyama, T. Konishi, T. Sudayama, N. L. Saini, M. Arita, H. Namatame, M. Taniguchi, N. Katayama, M. Nohara, H. Takagi, T. Mizokawa, and Y. Ohta: Phys. Rev. B **90** (2014) 155116.
15) T. Saitoh, Y. Yamashita, N. Todoroki, T. Kyômen, M. Itoh, M. Higashiguchi, M. Nakatake, and K. Shimada: J. Electron Spectrosc. Relat. Phenom. **144-147** (2005) 893.
16) M. M. Altarawneh, G.-W. Chern, N. Harrison, C. D. Batista, A. Uchida, M. Jaime, D. G. Rickel, S. A. Crooker, C. H. Mielke, J. B. Betts, J. F. Mitchell, and M. J. R. Hoch: Phys. Rev. Lett. **109** (2012) 037201.
17) A. Ikeda, T. Nomura, Y. H. Matsuda, A. Matsuo, K. Kindo, and K. Sato: Phys. Rev. B **93** (2016) 220401.
18) A. Ikeda, Y. H. Matsuda, and K. Sato: Phys. Rev. Lett. **125** (2020) 177202.
19) A. Sotnikov and J. Kuneš: Sci. Rep. **6** (2016) 30510.
20) J. Fujioka, Y. Yamasaki, H. Nakao, R. Kumai, Y. Murakami, M. Nakamura, M. Kawasaki, and Y. Tokura: Phys. Rev. Lett. **111** (2013) 027206.
21) J. Fujioka, Y. Yamasaki, A. Doi, H. Nakao, R. Kumai, Y. Murakami, M. Nakamura, M. Kawasaki, T. Arima, and Y. Tokura: Phys. Rev. B **92** (2015) 195115.
22) Y. Yamasaki, J. Fujioka, H. Nakao, J. Okamoto, T. Sudayama, Y. Murakami, M. Nakamura, M. Kawasaki, T. Arima, and Y. Tokura: J. Phys. Soc. Jpn. **85** (2016) 023704.
23) J. Kuneš: J. Phys.: Condens. Matter **27** (2015) 333201.
24) S. R. White: Phys. Rev. Lett. **69** (1992) 2863.
25) S. R. White: Phys. Rev. B **48** (1993) 10345.
26) Y. Kanamori, H. Matsueda, and S. Ishihara: Phys. Rev. Lett. **107** (2011) 167403.
27) P. Calabrese and J. Cardy: J. Stat. Mech. **2004** (2004) P06002.
28) S. Ejima, T. Kaneko, Y. Ohta, and H. Fehske: Phys. Rev. Lett. **112** (2014) 026401.